SECONDARY WAVES AND/OR THE "REFLECTION" FROM AND "TRANSMISSION" THROUGH
A CORONAL HOLE OF AN EXTREME ULTRAVIOLET WAVE ASSOCIATED WITH THE
2011 FEBRUARY 15 X2.2 FLARE OBSERVED WITH *SDO*/AIA AND *STEREO*/EUVI

OSCAR OLMEDO[1,5], ANGELOS VOURLIDAS[1], JIE ZHANG[2], AND XIN CHENG[3,4]
[1] Space Science Division, U.S. Naval Research Laboratory, Washington, DC 20375, USA; oscar.olmedo.ctr@nrl.navy.mil
[2] School of Physics, Astronomy and Computational Sciences, George Mason University, 4400 University Drive, Fairfax, VA 22030, USA
[3] School of Astronomy and Space Science, Nanjing University, Nanjing 210093, China
[4] Key Laboratory for Modern Astronomy and Astrophysics, Nanjing University, Ministry of Education, Nanjing 210093, China

ABSTRACT

For the first time, the kinematic evolution of a coronal wave over the entire solar surface is studied. Full Sun maps can be made by combining images from the *Solar Terrestrial Relations Observatory* satellites, *Ahead* and *Behind*, and the *Solar Dynamics Observatory*, thanks to the wide angular separation between them. We study the propagation of a coronal wave, also known as the "Extreme Ultraviolet Imaging Telescope" wave, and its interaction with a coronal hole (CH) resulting in secondary waves and/or reflection and transmission. We explore the possibility of the wave obeying the law of reflection. In a detailed example, we find that a loop arcade at the CH boundary cascades and oscillates as a result of the extreme ultraviolet (EUV) wave passage and triggers a wave directed eastward that appears to have reflected. We find that the speed of this wave decelerates to an asymptotic value, which is less than half of the primary EUV wave speed. Thanks to the full Sun coverage we are able to determine that part of the primary wave is transmitted through the CH. This is the first observation of its kind. The kinematic measurements of the reflected and transmitted wave tracks are consistent with a fast-mode magnetohydrodynamic wave interpretation. Eventually, all wave tracks decelerate and disappear at a distance. A possible scenario of the whole process is that the wave is initially driven by the expanding coronal mass ejection and subsequently decouples from the driver and then propagates at the local fast-mode speed.

Key words: Sun: corona – Sun: coronal mass ejections (CMEs) – Sun: flares – Sun: oscillations – Sun: UV radiation

Online-only material: animations, color figures

1. INTRODUCTION

Coronal waves are large-scale bright fronts that propagate over the solar surface, with speeds ranging from 50 to over 700 km s^{-1} (e.g., Thompson & Myers 2009; Warmuth & Mann 2011). These features have traditionally been called "Extreme Ultraviolet Imaging Telescope (EIT) waves," because they were first studied in detail (Moses et al. 1997; Thompson et al. 1998, 1999) with the EIT (Delaboudiniére et al. 1995). It is more appropriate to call them "extreme ultraviolet (EUV) waves" because they are observed in coronal EUV wavelengths. EUV waves have been associated with similar phenomena in other wavelengths, such as chromospheric He I (Vršnak et al. 2002; Gilbert & Holzer 2004; Gilbert et al. 2004), X-rays (Khan & Aurass 2002; Narukage et al. 2002; Hudson et al. 2003; Warmuth et al. 2005; Vršnak et al. 2006), and radio wavelengths (Klassen et al. 2000; Pohjolainen et al. 2001; Khan & Aurass 2002; Warmuth et al. 2004; Vršnak et al. 2005, 2006; White & Thompson 2005). They are also associated with coronal mass ejections (CMEs), flares, and type II radio burst (Biesecker et al. 2002; Cliver et al. 2005). Recent reviews on this topic can be found in, e.g., Wills-Davey & Attrill (2009), Gallagher & Long (2011), Warmuth (2010), Zhukov (2011), and Patsourakos & Vourlidas (2012). For the remainder of this paper, we will refer to this phenomena as a "coronal wave" or "wave front," which is appropriate because of their wave nature.

The interpretation of these waves has been a highly debated topic. Two broad scenarios have been proposed, that these are either true waves (magnetohydrodynamic (MHD) waves propagating in the corona) or pseudo-waves (a propagating front of an expanding structure, such as a CMEs outer envelope). Moreton waves (Moreton & Ramsey 1960) observed in Hα have been interpreted to be the chromospheric counterparts of fast-mode MHD coronal waves (Uchida 1968). Hence, it was natural to associate Moreton waves and "EIT waves" (e.g., Warmuth et al. 2004). Much evidence has been put forth for the MHD wave interpretation, as a fast-mode wave (e.g., Wills-Davey & Thompson 1999; Wang 2000; Wu et al. 2001; Ofman & Thompson 2002; Patsourakos & Vourlidas 2009; Patsourakos et al. 2009; Schmidt & Ofman 2010), a slow-mode wave (Wang et al. 2009), or soliton wave (Wills-Davey et al. 2007). The pseudo-wave interpretation proposes several mechanisms all associated with the large-scale structure of the associated CME. One such pseudo-wave is the propagating reconnection front (Attrill et al. 2007a, 2007b; van Driel-Gesztelyi et al. 2008), in which, as the CME is expanding, it interacts with the smaller scale loops in the vicinity via reconnection to produce heat and enhanced EUV intensity. Another possible pseudo-wave mechanism is the disk projection of large-scale current shells that surround the expanding flux-rope core of a CME (Delannée et al. 2008). Joule heating and/or plasma compression can occur at these shells and lead to enhanced intensities. Yet another pseudo-wave mechanism is the plasma compression due to the successive openings of the overlying magnetic fields as the CME is expanding (Chen et al. 2002, 2005). Patsourakos et al. (2009) compiled a list of several observational tests for comparing the wave and pseudo-wave explanations, upon applying these tests to one event they concluded in favor of a fast-mode wave

[5] NRC Research Associate at NRL.

interpretation and state that this wave is "probably" triggered by the expansion of the loops associated with the CME—in other words, that it is driven by the CME. Finally, another point of view takes on a hybrid of wave and pseudo-wave interpretations (Chen et al. 2002, 2005; Zhukov & Auchére 2004; Cohen et al. 2009; Chen & Wu 2011; Downs et al. 2011; Cheng et al. 2012). In this hybrid, view a CMEs outer envelope is the pseudo-wave that can drive a fast-mode wave ahead, which subsequently evolves freely over the solar surface once the CME has propagated sufficiently away from the Sun. This emerging hybrid view shows the most promise for a complete description of coronal waves as it can account for most (if not all) observational features.

The controversy seems to stem largely from ambiguities in the observed features due to limited spatial or temporal sampling. Recent ultrahigh-cadence observations show clearly the formation of a shock in the EUV corona (Liu et al. 2010; Kozarev et al. 2011; Ma et al. 2011; Cheng et al. 2012) providing strong support for the fast-mode interpretation. Further, the reflection of coronal waves at coronal hole (CH) boundaries is especially difficult to reconcile with a pseudo-wave mechanism. The first reported observation of a reflection of a coronal wave was associated with the event of 2007 May 19 (Long et al. 2008; Veronig et al. 2008; Gopalswamy et al. 2009), and more recently the 2011 June 7 event (Li et al. 2012). Gopalswamy et al. (2009) studied the 2007 May 19 coronal wave event in detail and reported the reflection of the primary wave in three directions from a nearby CH west of the flaring active region, and possibly a fourth by a CH to the south. To perform this analysis they used running differenced images to show this effect (the same technique was also used by Li et al. (2012) to show an example of reflection). In the technique of running difference, each image in a sequence of images is subtracted from the previous image to enhance moving features or intensity variations. The use of this technique caused some controversy because it can produce misleading wave-like effects. Upon reanalysis of this event, Attrill (2010) showed that using running difference caused such misleading effects, or "optical illusions," and further comparison with a base differencing technique concluded that the "wave" does not in fact reflect from the CH boundary. In base difference, one selects a pre-event image and systematically subtracts that image from all the images in the sequence. Zhukov (2011) comments that using this technique is also flawed in the case of a wave reflected back toward the eruption site because the background intensity over which the reflected wave propagates may have changed due to EUV dimming, making the wave more difficult to detect. To explain what Gopalswamy et al. (2009) report as "reflection," Attrill (2010) invokes hot plasma channeled along coronal loops in the opposite direction of the "wave," a secondary event (presumably occurring very soon after the initial event, as suggested by the associated double-CME event), and/or a rotation of the "wave" due to local inhomogeneities of the fast-mode MHD wave speed. Therefore, the question of reflection remains open, especially since the techniques used to identify reflection have been called to question. Here, we provide new observations of an event in which reflection could be a possible explanation, as the trajectory of the reflected wave seems to obey the law of reflection. In one example, we show that there is a spatial and temporal correlation between the wave, which appears to have reflected from the CH boundary, and the oscillation of a loop arcade at the CH boundary aligned with the trajectory of the reflected wave. The loops in the arcade are triggered to oscillate

one by one as the primary (or incident) wave reaches each individual loop, thereby giving the appearance of the oscillation of the first loop triggering the oscillation of the next loop and so forth in what appears to resemble a cascade. However, the observations cannot conclusively determine whether the wave is in fact a true reflection or launched by the loop arcade. Excitation of coronal loop oscillations by the primary coronal wave has been reported in the literature (e.g., Wills-Davey & Thompson 1999; Ofman & Thompson 2002; Hudson & Warmuth 2004; Ofman 2007; Aschwanden & Schrijver 2011), though what is novel about this observation is the fact that an entire loop arcade oscillates and that the cascading speed was found to be related to the oblique angle at which the primary wave reached the arcade.

In addition, we report the first detection of wave transmission through a CH, as previous observations seemed to indicate that coronal waves were stopped at the boundaries of CHs (e.g., Thompson et al. 1998; Veronig et al. 2006). Both reflection and transmission have been predicted in recent MHD simulations of fast-mode coronal waves (Schmidt & Ofman 2010). Schmidt & Ofman (2010) identify in their simulations "secondary waves," which seem to describe both reflection and transmission waves. For the sake of generality, we use the same approach and define a "secondary wave" as any other observed wave induced (either directly or indirectly) by the primary wave including apparent reflected and transmitted waves. For example, we call the wave triggered by the cascading loop arcade at the CH boundary a secondary wave.

Our paper is organized as follows. In Section 2, we introduce the multi-viewpoint and multi-wavelength space based EUV observations of the Sun and the full Sun EUV maps we use for analyzing the wave propagation on a global scale. In Section 3, we discuss our kinematic analysis of the wave reflection and transmission. We conclude in Section 4.

2. OBSERVATIONS AND METHODOLOGY

In this paper, we study the coronal wave associated with the X2.2 flare and CME of 2011 February 15, with a NOAA-reported[6] flare onset time of 01:44 UT and peak time of 01:56 UT. This event has also been studied by other authors who have looked into the photospheric, magnetic, and helioseismic evolution during the flare (Kosovichev 2011; Schrijver et al. 2011; Beauregard et al. 2012; Gosain 2012; Jiang et al. 2012; Petrie 2012; Wang et al. 2012). An extensive study of this event was recently made by Schrijver et al. (2011) who discussed the coronal wave thermal properties, coronal loop evolution, and CME eruption and its connection to the coronal wave. The primary focus of the work of Schrijver et al. (2011) was the initial stages of the eruption (up to ∼02:00 UT), and based on a zero-β MHD simulation studied the pseudo-wave component of this event, namely, the outer envelope of the expanding CME, which they interpret to be a current shell (Delannée et al. 2008). Taking the hybrid interpretation, the work presented herein will focus on the freely propagating fast-mode wave component initially driven by the CME. This work, together with the work of Schrijver et al. (2011), gives a complete hybrid picture of the coronal wave associated with this event.

We combine observations from the Extreme Ultraviolet Imaging Telescope (EUVI; Wuelser et al. 2004) aboard the *Solar Terrestrial Relations Observatory* (*STEREO*; Kaiser et al. 2008), part of the Sun–Earth Connection Coronal and Heliospheric

---

[6] NOAA 2011 events: ftp://ftp.ngdc.noaa.gov/STP/SOLAR_DATA/ SOLAR_FLARES/FLARES_XRAY/2011/XRAY2011
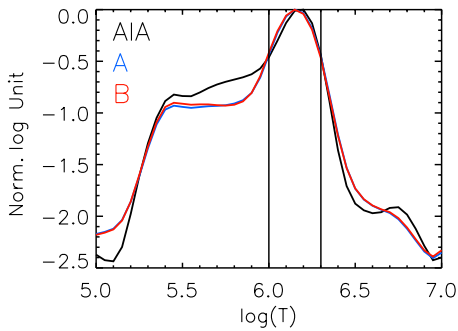
Figure 1. Temperature response of the AIA 193 Å, EUVI-A 195 Å, and EUVI-B 195 Å passbands in peak-normalized log units. The vertical lines at 6.0 and 6.3 correspond to 1 and 2 MK, respectively.

(A color version of this figure is available in the online journal.)

Investigation (SECCHI; Howard et al. 2008), and the Atmospheric Imaging Assembly (AIA; Lemen et al. 2011) on board the *Solar Dynamics Observatory* (*SDO*). These three EUV full disk imagers give us the capability to image the entire EUV Sun instantaneously. We make maps of the full Sun by combining AIA 193 Å images, taken from the vantage point at Earth, with EUVI 195 Å observations from the vantage points of the twin *STEREO* satellites, *Ahead* (*A*) and *Behind* (*B*). Figure 1 shows the temperature response of the three instruments. The black line corresponds to AIA 193 Å, the blue to EUVI-A 195 Å, and the red to EUVI-B 195 Å. The response of EUVI-A and EUVI-B is essentially identical. Comparing AIA with EUVI, there is good overlap over 1–2 MK, with peak temperatures of 1.6 MK and 1.5 MK, respectively. It is known that coronal waves can be clearly observed in a temperature range between 1 and 2 MK (e.g., Patsourakos et al. 2009), and therefore these combined observations are well suited for studying coronal waves.

The *STEREO-A* satellite orbits ahead of the Earth and the *STEREO-B* behind the Earth, both with orbit radius approximately equal to 1 AU around the Sun. Immediately before the time of the event, at 01:35 UT on 2011 February 15, the separation angle between the Earth and the *STEREO-A* satellite was 86°.75 and the *STEREO-B* satellite was 94°.08. The separation angle between the *STEREO* satellites was therefore ∼180°. With the *STEREO* observations alone it is possible to make maps of the entire Sun, with the drawback that the limb observations will suffer from projection effect, due to the curvature of the Sun. Therefore, on full Sun maps where the limbs of *STEREO-A* and *B* overlap (or the "seams"), the quality of the observations of low-lying features will be relatively poor. We can overcome this problem, at least for the "seam" aligned with the Earth, by replacing it with observations from AIA. A map of the Sun using these three observations is made by interpolating the images, which are in helioprojective coordinates, to heliographic coordinates, assuming that the radius is equal to one solar radius, and then onto a longitude/latitude Cartesian grid (Thompson 2006). In regions on the map where multiple viewpoints overlap, the observation at each latitude/longitude position that is close to the Sun center within each respective instruments FOV, in helioprojective coordinates, is chosen. The seams are the exact position where the distance to the Sun center within the FOV of the two instruments, in helioprojective coordinates, is equal.

The full Sun maps are then transformed into Stonyhurst coordinates with a fixed reference time. This is the same as shifting Carrington coordinates such that the longitude of the solar central meridian as seen from the Earth, at the fixed reference time, is centered on the map and corresponds to 0°.

Note that the Stonyhurst and Carrington latitudes are equal. The longitudinal axis is in Stonyhurst units from −180° to +180°. All subsequent frames are de-rotated to be aligned with the reference time. In this way, long-lived features (such as active regions, and CHs) with respect to the event will remain fixed on the map as the Sun rotates. For the 2011 February 15 event, the reference time is taken to be 01:35 UT and the solar central meridian Carrington longitude (*L*0) is +21°.9. Figure 2 shows the transformation from the individual AIA, EUVI-A, and EUVI-B images (top row) to the map (bottom). The flare kernel site's location is at Stonyhurst longitude 12°.1 (Carrington longitude 34°) and latitude −20°. Overlaid onto the AIA, EUVI-A, and EUVI-B FOV is a longitude/latitude grid. The vertical lines on the map (bottom) correspond to the central meridians, at 01:35 UT, of AIA (0°), EUVI-A (+86°), and EUVI-B (−94°). For the 2011 February 15 event, a new map is made every 5 minutes starting at 01:35 UT until the end of the event, which we define as the time when the propagating wave becomes too faint to track (∼03:35 UT). When making these maps, we are limited to the lowest cadence of the three instruments. EUVI typically has a cadence between 2.5 and 10 minutes for normal operations, and AIA a cadence of 12 s. On February 15, the cadence of EUVI-A and EUVI-B 195 Å was 5 minutes. For the present study, the 5 minute cadence is sufficient.

The CH boundary is determined manual by comparing the three vantage point observations, it is drawn in white in Figure 2. We also tried using a threshold segmentation method to automatically find the CH boundary, as was done by Gopalswamy et al. (2009), but found that the segmented boundary from one vantage point did not appropriately outline the CH as seen from a different vantage point.

To analyze the kinematics and other effects we construct stack plots. To get a sense of the thermal changes in the corona during the passage of the front, we compare observations from four AIA instrument channels sensitive to nominal coronal temperatures on the order of 10^6 MK. The AIA instrument channels used in this study, from coolest to hottest peak temperature response, were AIA 171 Å (Fe IX) at 0.6 MK, AIA 193 Å (Fe XII) at 1.5 MK, AIA 211 Å (Fe XIV) at 2.0 MK, and AIA 335 Å (Fe XVI) at 2.5 MK (O'Dwyer et al. 2010; Lemen et al. 2011). AIA has an automatic exposure control (AEC) in cases of intense events, such as the 2011 February 15 flare, that reduces the exposure every other image but also reduces the signal-to-noise ratio (see Schrijver et al. 2011 for more discussion on AEC during this event). For consistency, we used only AIA images that had the standard exposure time, which for AIA 171 Å and 193 Å is ∼2 s, and 211 Å and 335 Å is ∼2.9 s. If non-standard exposure time images were included in the stack plots it would cause vertical stripes to be seen corresponding to image pairs used for running/base ratio that had different exposure times on the account of the images having different background noise distributions. Therefore, the cadence of AIA data used in this study was ∼24 s.

3. RESULTS

3.1. Kinematics of the Primary Wave

In this section, we present the measurement of the kinematics of the primary wave and compare AIA with off-limb EUVI observations. To make a direct comparison, we make a stack plot of a great circle ground track slice of width 36.6 arcsec off set from the meridian at the equator by 9°, labeled as "B" in Figure 3. Figure 4 shows the corresponding stack plot made
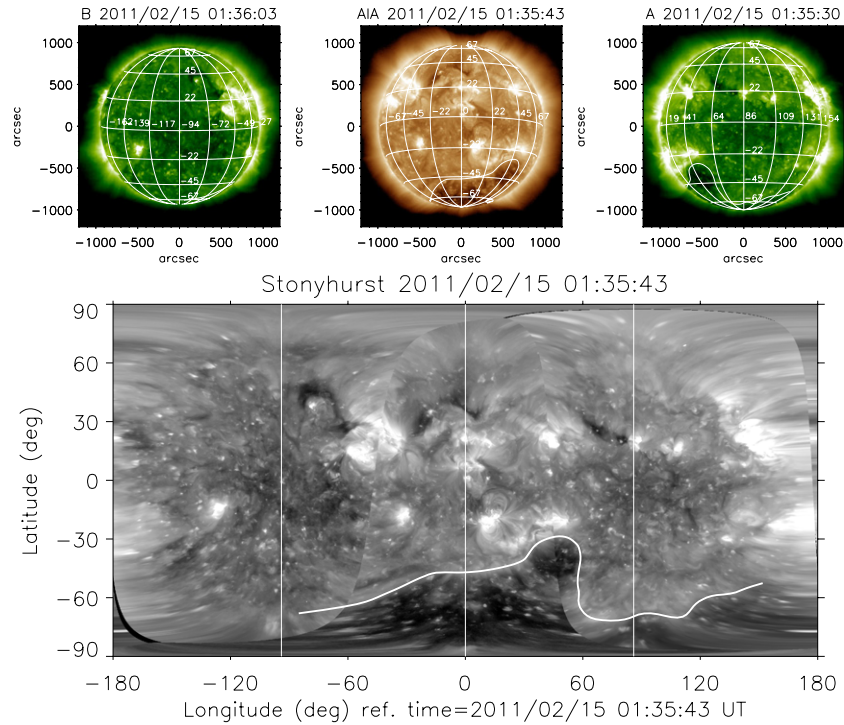
Figure 2. Combining the three observations from AIA 193 Å (top center), EUVI-A 195 Å (top right), and EUVI-B 195 Å (top left) to make a full Sun map (bottom). Top panel shows the Sun from the three viewpoints at approximately the same reference time of 2011 February 15 ~01:35 UT. The bottom panel is the map of the combined three images in Stonyhurst units. The coronal hole boundary, as outlined using the AIA 193 Å image, is projected onto the map. The vertical white lines in the map correspond to the central meridians of EUVI-B, AIA, and EUVI-A with Stonyhurst Longitude at 01:35 UT of $-94°$, $0°$, and $86°$, respectively.

(A color version of this figure is available in the online journal.)
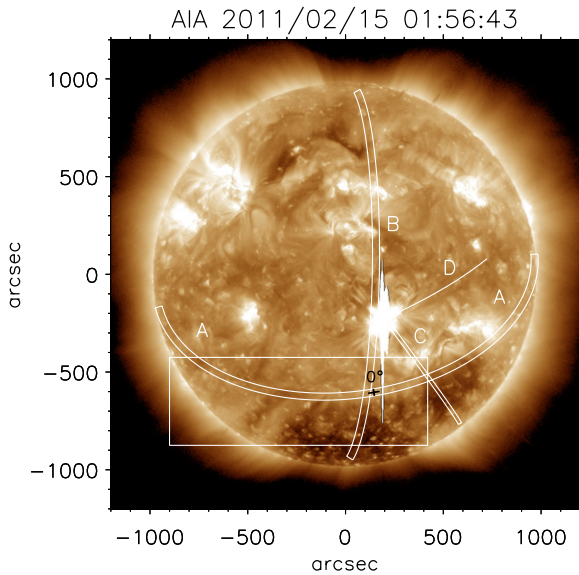
Figure 3. SDO/AIA 193 Å image showing the ground track slices made for this study. Note that the tracks follow great circles. The location of $0°$ along slice "A" is marked by a black "+."

(A color version of this figure is available in the online journal.)

with the four AIA channels, where the top row is the 4.8 minute running ratio, and the bottom row is the base ratio, with the base time at 01:35 UT. The axes are in heliographic coordinates where the origin is the Earth-facing equator, positive values are toward the north, and negative toward the south—in this way we can have a more direct comparison with the off-limb EUVI observations. Figure 5 shows EUVI-A and EUVI-B 195 Å base

ratio stack plots, with base time at 01:35 UT, of a concentric circle slice around the Sun at a radius of 1.15 $R_\odot$ and of width 50 arcsec. Figure 6 (middle row) shows the concentric circle arc slices overlaid on the EUVI-A and EUVI-B images. We first focus on the top row of Figure 4 in which the velocity of the front is measured as it propagates toward the north and south. The velocity measured projected onto the surface toward the north was 720 ± 20 km s^{-1} and to the south was 740 ± 30 km s^{-1}. The error was estimated from making the fit 10 times by placing two points along the front and deriving the velocity. The velocity measured toward the north is in agreement with Schrijver et al. (2011) that reported 730 km s^{-1}. Although the north/south velocities are approximately equal, their tracks seem to be offset in time by ~2 minutes with the south ahead of the north. This asymmetry could be due a projection effect, considering that the southern track is closer to the limb. The red horizontal line at $-44°$ is the CH boundary toward the south of the flare site. An interesting feature in this stack plot is an apparent transmission of the wave front through the CH propagating at the same velocity as the primary wave. This feature is most evidently seen in AIA 193 Å and AIA 211 Å observations. As can be seen in the AIA 193 Å running ratio movie (available in the online journal), the transmission occurs all along the CH boundary. Though we must be cautious because it may be that what we are seeing is due to a projection effect of the wave deflected above the CH. We return to this topic in Section 3.3.

The two dashed horizontal lines in Figure 4 are positions identified by Schrijver et al. (2011) as the location of the post-CME flanks, which we interpret as the angular extent of the CME. In the work of Schrijver et al. (2011), the velocity reported to the north is fitted only up to the northern post-CME flank at $20°$. We note that between ~$15°$ and ~$40°$ the slice passes
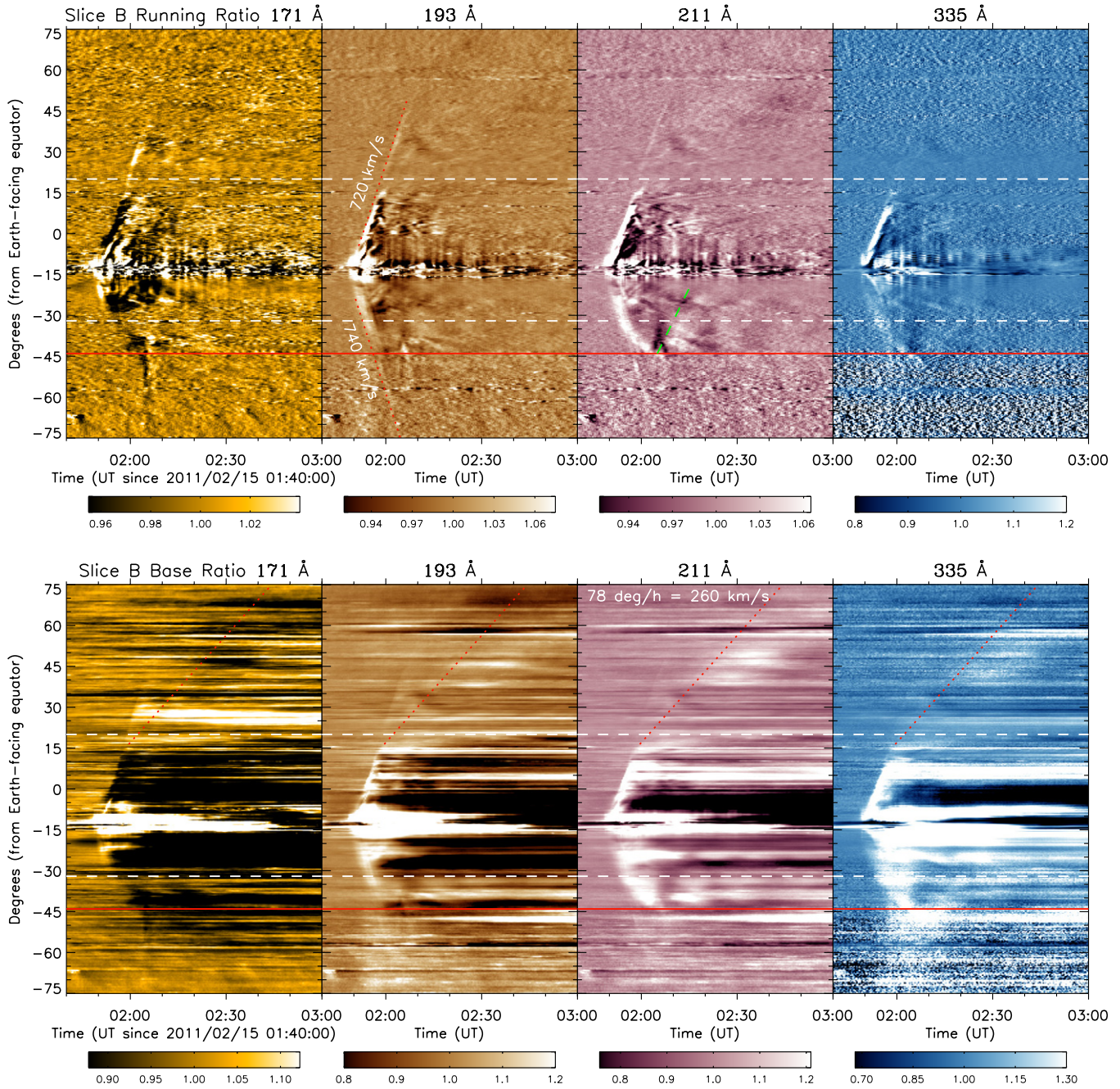
Figure 4. Slice "B" lies 9° from the meridian at the equator. All four AIA channels are shown here. The top panel shows running ratio stack plots, and the bottom shows base ratio. This figure demonstrates the bifurcation of the wave into a fast (shown with the running ratio plots) and slow (shown with the base ratio plots) component. The horizontal red line at −44° is the coronal hole boundary and the two horizontal dashed lines at −32° and 20° are the post-CME flanks.
(A color version of this figure is available in the online journal.)

through part of an active region. However, our extended plot reveals bifurcation of the front into fast and slow components. The fast component can be seen in both running ratio and base ratio stack plots in Figure 4. The front, as observed in AIA 171 Å, is initially seen as a dimming and an enhancement in the other three AIA channels. This observation can be explained as an adiabatically heated plasma due to a compression front (e.g., Downs et al. 2012). On the other hand, beyond 20° the front is observed as an enhancement in the four AIA channels. This is interpreted as maybe due to either a density enhancement and/or a transverse/kink-mode wave traveling along the loops and not a temperature effect (see AIA 193 Å movie associated with Figure 7).

The slow component is identified in the base ratio stack plots and is most prominently seen in AIA 211 Å. The front is faintly observed in AIA 193 and 335 Å, and faintly observed as a dimming in AIA 171 Å indicating adiabatic heating. We attempt to measure the velocity and find a value of 260 ± 20 km s^{-1}. We compare AIA observations with off-limb EUVI observations in Figure 5. The EUVI-A/B stack plots look essentially identical because they are observing almost exactly 90° from the Earth-facing disk center in opposite directions. Again, the horizontal red line at −44° is the location of the CH boundary and the two dashed horizontal lines are the post-CME flanks. The velocity fits for the fast and slow components found with AIA are overplotted onto the EUVI plots (dotted red lines) and
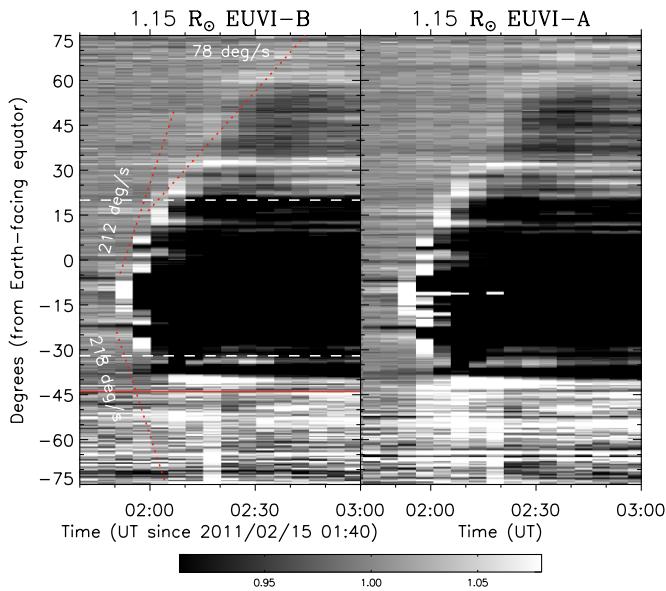
Figure 5. Above the limb base ratio stack plot with EUVI-A 195 Å and EUVI-B 195 Å observations of concentric circles around the Sun at 1.15 $R_\odot$. The horizontal red line at $-44°$ is the coronal hole boundary and the two horizontal dashed lines at $-32°$ and $20°$ are the post-CME flanks.

(A color version of this figure is available in the online journal.)

appear reasonable considering the lower cadence of EUVI. The values written on the plot have been converted to degrees per hour, where 260 km s^{-1} = 78° hr^{-1} is the slow component, 730 km s^{-1} = 212° hr^{-1} is the fast component toward the north, and 740 km s^{-1} = 218° hr^{-1} is the velocity toward the south. The region below the slow component shows a weak dimming in both EUVI 195 Å stack plots. The intensity of the dimming is much smaller than the dimming caused by the evacuation of material under the main body of the CME (within the dashed lines in the figure). The relatively long duration (at least 40 minutes) of the dimming, however, suggests that it might be the result of mass evacuation rather than mass displacement. Therefore, the lateral CME expansion and consequent coronal mass outflow do not stop at ∼20° north of the flaring site but continue northward to ∼60° but at a much diminished rate. An alternative explanation could be that after ∼20°, the location of the CME flank, a fast-mode wave is launched at the local fast-mode speed of 260 km s^{-1} and that the dimming in EUVI is due to heating of the tenuous plasma. This is a plausible explanation considering that this velocity is comparable to the fast-mode speeds measured in other parts of the Sun associated with this event. It is also consistent with the hybrid interpretation of coronal waves because the slow component could be the fast-mode wave left traveling close to the solar surface that is no longer being driven by the CME, which has propagated radially away. The fact that the AIA observations show an enhancement and EUVI observations show a dimming along that track can be understood as a line of sight effect. The AIA telescopes look straight down the outflowing material while in the EUVI imagers look above the limb. In any case, the dimming region in the EUVI stack plots exactly corresponds to the same region of enhancement in AIA indicating that we are tracking the same feature. Note that this feature is not observed toward the south where the CH lies. Obviously, the CME cannot expand into the CH and hence no outflowing material is observed, on the other hand any heating by the fast-mode wave traveling

through the CH may not be observed because of the low density there.

3.2. Kinematics of the "Reflected Wave" Front

We have applied the technique of making full Sun maps, as described in Section 2, to a sequence of images from 01:30 to 03:35 UT with a cadence of 5 minutes. Running ratio images were compared with base ratio images (using a base image at 01:35 UT) and it was found that utilizing either technique does not change our results. Figure 6 shows a sample of running ratio images from the sequence. Movies of the sequence (full Sun map as well as AIA 193 Å, EUVI-A, and EUVI-B) are provided in the online journal. The left column is EUVI-B, the center is the map, and the right is EUVI-A. The CH boundary (red) is projected onto the FOV of each image.

Since we are interested in the possibility of wave "reflection" from CH boundaries, we perform a ray trace analysis. This is strictly for visualization purposes to guide the eye to the motion of the propagating front. We consider six trajectories originating from the flare site, following great circle paths, and terminating at the CH boundary. Three of the paths extend to the east and three to the west of the source region. The incident and reflected angle is calculated with respect to the smoothed CH boundary. Then the six trajectories are extended along the reflected path. Note that these are our predicted paths for the trajectory of the coronal wave obeying the law of reflection purely under the assumption that the incident and reflected angles are equal. The eastern reflection is more easily observed than the western one, which appears more diffused. After ∼2:45 UT, the western reflection becomes too diffuse to be seen. The eastern reflection is visible until ∼3:20 UT. Looking carefully at the rays drawn, one notices that initially the three rays to the east and to the west appear to almost overlap, yet in the FOV of the EUVI-A and EUVI-B the reflected rays diverge greatly. This is due to the convexity of the CH boundary and is sensitive to how that boundary is drawn. In any case, the rays drawn were carefully chosen by adjusting the incident angle and the position at the CH boundary where the reflection takes place to emphasize the trajectory of the front within the FOV of EUVI-A and EUVI-B.

Next, we placed a great circle path chosen to follow the trajectory of the wave front in the FOV of EUVI-B and extended it through the FOV of AIA and EUVI-A. This path was made independently from the ray tracing analysis described. It was coincidentally found that this path was aligned nearly parallel with the reflected ray trace in both the EUVI-A and EUVI-B FOV (Figure 6, full Sun map, middle panel) for this reason we call this the "reflected" wave. Another interesting find is that this path is aligned with the CH boundary. Close inspection reveals the existence of a loop arcade straddling this part of the CH boundary, a cutout of the loop region is shown in Figure 7. The kinematics of the wave and the role of the loops are further studied by making stack plots using the AIA and EUVI instruments along this great circle path. This stack plot is shown in Figure 8, and is directly comparable to Figure 6. The left panel is AIA 193 Å 4.8 minutes running ratio, and the right panel shows both EUVI-A and EUVI-B with 5 minutes running ratio. Here, we have removed the seam and instead show all of the available spatial observation to directly compare what is seen within the FOV of the three instruments. The width of the slice used to make the stack plot in the AIA FOV was 36.6 arcsec, shown in Figure 3 labeled as "A," and the width of the slice in the EUVI FOV was 50 arcsec. Zero degrees in Figure 8
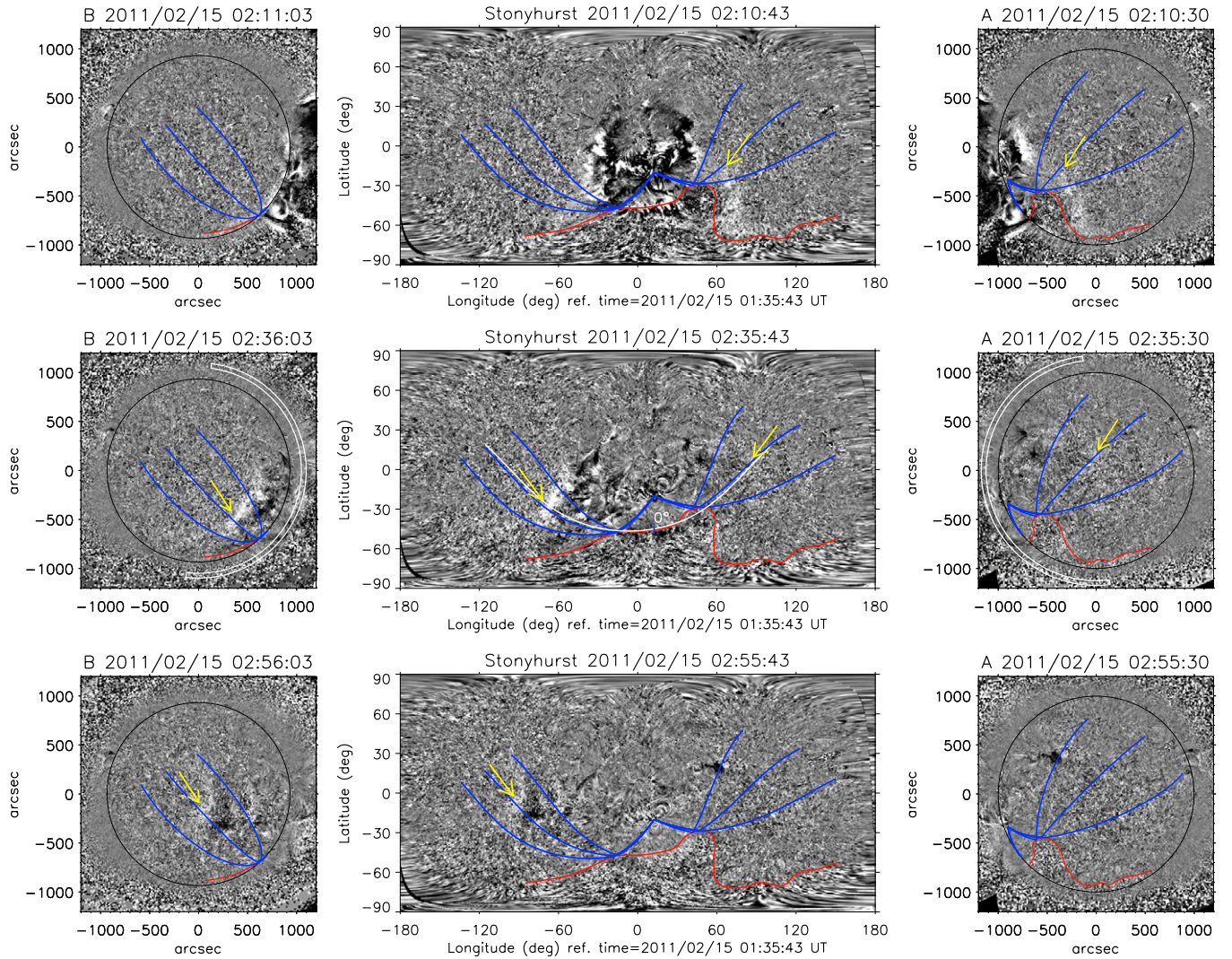
Figure 6. Sequence of running ratio frames showing the evolution of the coronal wave at different time steps. The left column is EUVI-B 195 Å, the right column is EUVI-A 195 Å, and the center column is the full Sun map that combine EUVI-A and EUVI-B with AIA 193 Å. Yellow arrows indicate the wave front. Blue lines are the predicted trajectory, indicating the reflection from the coronal hole boundary. The red line is the coronal hole outline. The white line drawn on the full Sun map of 02:35 UT (center) is slice A.

(Animations and a color version of this figure are available in the online journal.)

is marked in Figures 6 (middle panel) and 3. The full angular extent of the wave into the FOV of EUVI-A and EUVI-B along this path is ≳200° (Figure 8, right panel). If measured from the flare site, the extent to the west (into the FOV of EUVI-A) is ∼80° and to the east (into the FOV of EUVI-B) is ∼120°, therefore the angular extent as measured from the flare site is also ≳200°.

Further out in the FOV of EUVI-A and EUVI-B (Figure 8, right panel), the velocity of the "reflected" wave appears to be linear. To the east, into the FOV of EUVI-B the velocity was found to be 280 ± 10 km s^{-1}, and to the west into the FOV of EUVI-A, 380 ± 25 km s^{-1}. Again, the error was estimated from making the fit 10 times by placing two points along the front and deriving the velocity. These values resemble those found by Schrijver et al. (2011; 270 ± 35 km s^{-1} and 340 ± 35 km s^{-1} to the east and west, respectively), though it should be noted that they just estimated the velocity by finding the Carrington longitudinal position of the front at 03:00 UT ($-60°$ and $+105°$ to the east and west, respectively) and estimated the velocity to reach that longitude from the flare site longitude.

Comparing what is observed in AIA versus EUVI-A, we see that the fit in the FOV of EUVI-A does not exactly correspond to what is seen in AIA, unlike between AIA and EUVI-B. A plausible explanation is that the wave front (or part of the wave front) observed is at some height in the corona and not close to the surface, and so will appear different depending on the perspective. Alternatively, in the FOV of AIA slice "A" is overlaid over an active region loop system, with loops that are projecting into the corona, and as the primary wave interacts with these loops intensity enhancement in running ratio images could be due to oscillations and/or mass motions occurring not close to the surface but at a different height along the loop. On the other hand, between AIA and EUVI-B the wave passes over the quiet Sun where there is no active region or loop system. It is known that observations of a coronal wave from multiple viewpoints should look alike as the wave propagates away from its origin (Ma et al. 2009) given that it does not interact with other coronal structures. This is an indication that the wave observed is close to the solar surface and that what we see between AIA and EUVI-B is the same feature.
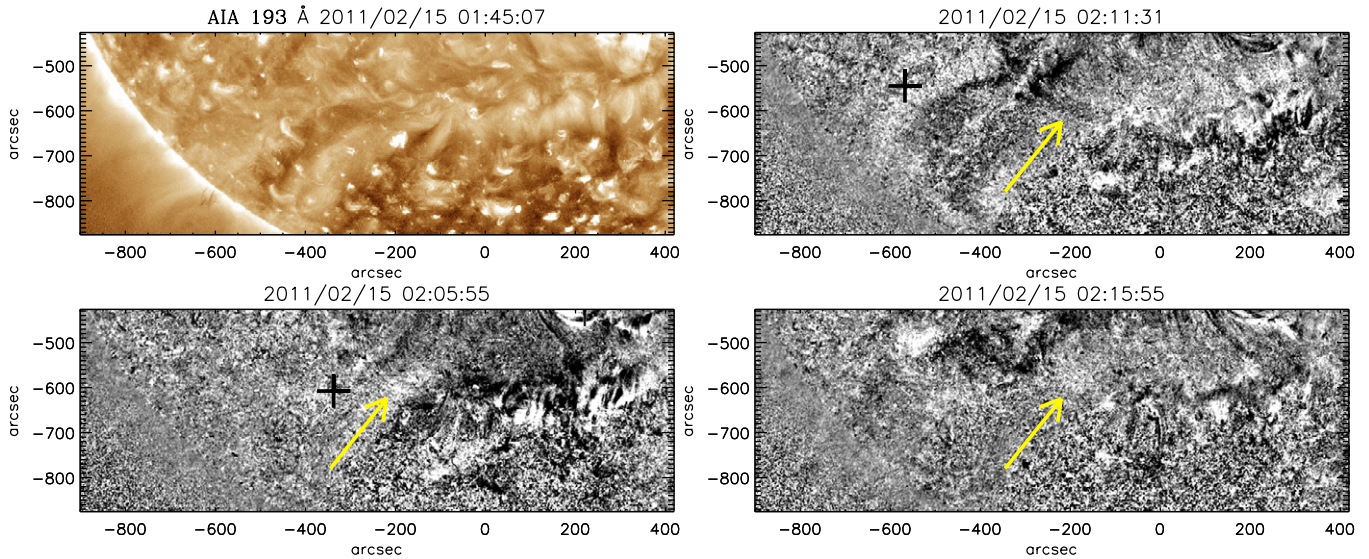
Figure 7. Cutout region, indicated by the rectangle in Figure 3 showing the loops at the coronal hole boundary. Top left panel is an image enhanced using a wavelet technique. The arrows point to secondary waves apparently launched by the oscillating loop arcade. The black "+" at 02:05 UT and 02:11 UT indicates the position of the wave front as seen along slice "A" (see Figure 9).

(Animations and a color version of this figure are available in the online journal.).
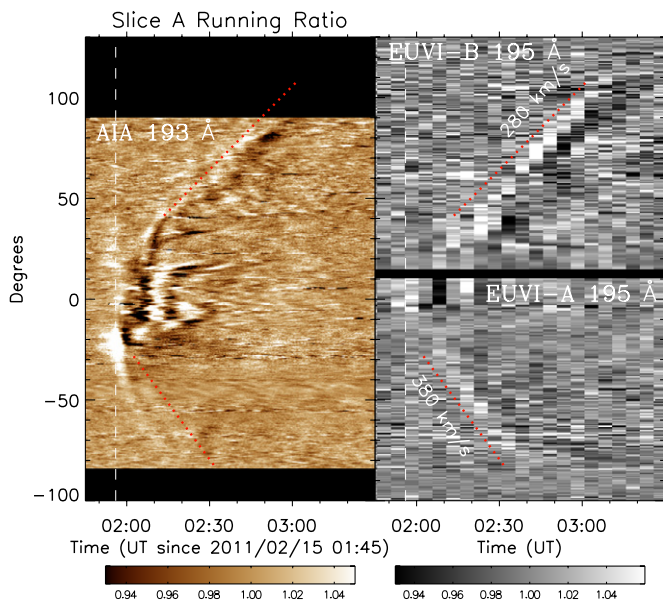
Figure 8. Ground track slice "A" that spans 230° across the Sun. On the left is the AIA 193 Å stack plot and on right are the EUVI-A 195 Å (bottom portion) and EUVI-B 195 Å (top portion) stack plots. The vertical dashed line at 01:56 UT is the flare peak time.
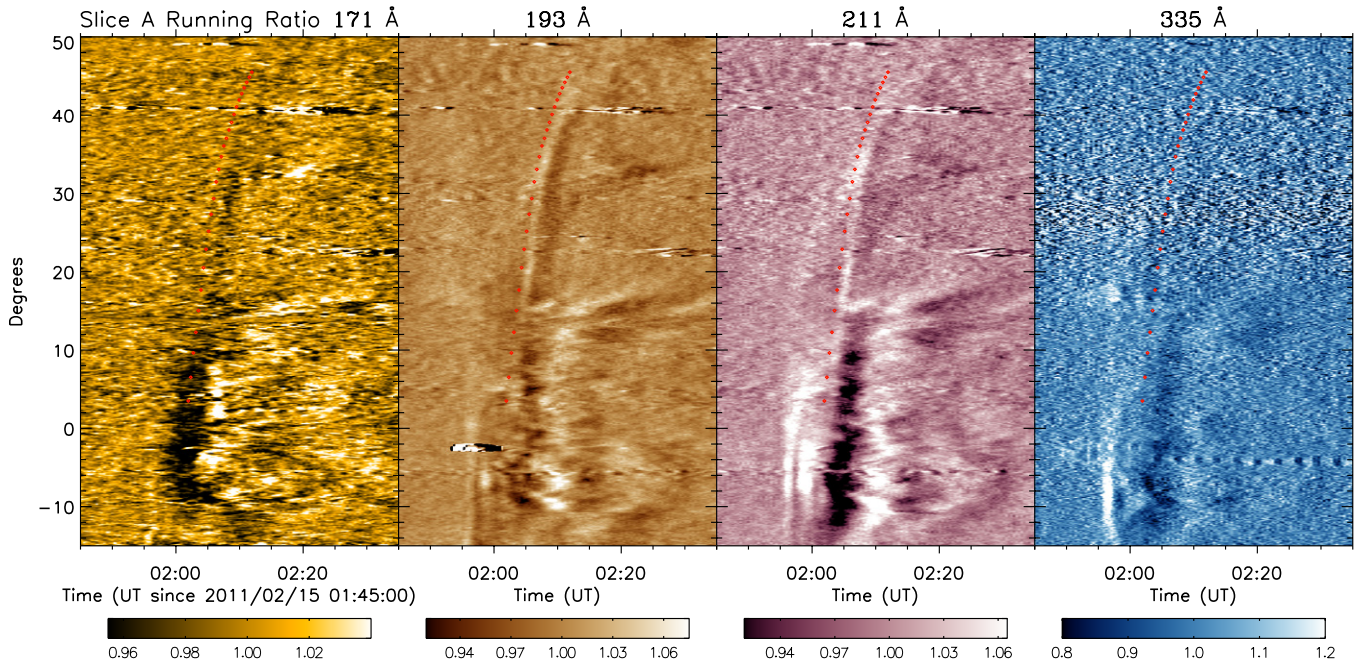
(A color version of this figure is available in the online journal.)

Next, we look into the loop arcade that straddles the CH boundary, shown in the cutout in Figure 7 (top left) after being enhanced with a wavelet method (Stenborg & Cobelli 2003). The other panels of Figure 7 are a sequence of 1.2 minute running ratio images. The enhanced movie (provided in the online journal) of the loop arcade reveals the response of the arcade to the primary wave. The loops within the arcade are seen to oscillate perpendicular to the primary wave, then quickly damp after about two periods. It is difficult to distinguish if the loops are oscillating transversely or with the kink mode or a combination of both as no individual loop can be identified within the arcade. Furthermore, the loop arcade is seen close to

the central meridian so only the tops of the loops are observed. A similar case of a loop excited to oscillation by a primary fast-mode wave has recently been reported using SDO/AIA observations by Aschwanden & Schrijver (2011). The cascading and oscillating loop arcade can be seen in the AIA stack plot of Figure 8 (left panel) between $-15°$ and $18°$. We estimate the period to be about 10 minutes, which is consistent with measured periods of transverse loop oscillations (e.g., White & Verwichte 2012). Figure 9 shows a close-up of the area between $-15°$ and $50°$ of Figure 8 using 1.2 minutes instead of 4.8 minutes running ratio. Using AIA 193 Å and 211 Å we manually track the wave front feature that extends beyond the loop arcade. We interpret this feature as a wave triggered by the cascading loop arcade, which propagates toward EUVI-B (also see the AIA 193 Å running ratio movie). We propose that this is the origin of the wave which we are calling the "reflected" wave. Figure 10 shows the kinematics of this wave, we approximate a conservative measure error of 0°.5. From 0° to 18° or from 02:02 UT to 02:04 UT, the speed has an average value of $\sim$1400 km s^{-1}. This is the velocity at which the loop arcade cascades in response to the primary wave, which reached the arcade at an oblique angle. Between 02:04 UT and 02:06 UT, the wave front crosses a filament channel that is running parallel with the CH boundary. This filament is connected to the prominence that is seen over the southeast (SE) limb in Figure 7 (top left). After 02:06, the wave front subsequently decelerates to a velocity range of a few hundred km s^{-1}, which is consistent with the velocity measured in the FOV of EUVI-B. This front is clearly seen in Figure 7 (top right) and the black "+" mark is the position of the front as measured in the stack plot shown in Figure 9. There appears to be another secondary wave that emanates from the CH boundary occurring $\sim$10 minutes after the primary wave has past. It can be seen in the AIA 193 Å running ratio movie between 02:10 UT and 02:30 UT propagating in the northeast (NE) direction from the loop arcade (arrows in Figure 7). Its appearance seems to outline a loop system overlying the filament channel and oscillates with a period of $\sim$10 minutes just like the loop arcade.

We note an effect that can arise in stack plots that are aligned between the active region that launched the coronal wave and

Figure 9. Close-up view of slice "A" stack plot in all four AIA channels to more clearly show the secondary wave triggered by the cascading loops. The measured points are indicated by the red dots.

(A color version of this figure is available in the online journal.)
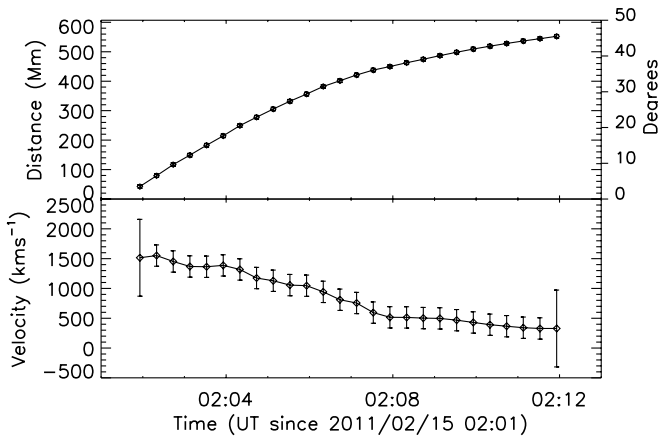
Figure 10. Distance–time and velocity plots of the triggered wave. An error of 0°.5 was estimated for the distance measurement.

the reflecting CH surface, such as slice "B." Looking closely at the AIA 211 Å running ratio stack plot in Figure 4 (top) in the region between $-15°$ and $-45°$, there appears a feature after ∼02:05 UT which might be interpreted as a reflection. It has been highlighted in the figure as a dashed (green) line. this feature is in fact related to the oscillating loops at the CH boundary. Other examples in the literature of a stack plot aligned between the active region that launched the coronal wave and the reflecting CH surface are those presented by Gopalswamy et al. (2009) and Li et al. (2012). Upon close inspection of that region, Attrill (2010) explains that the reported reflection can be attributed to hot plasma channeled along loops in the direction back toward the active region. This scenario resembles the observation of the loops above the filament channel that we described above. If we had made a stack plot over this region it would in fact resemble a reflection. Just to be clear, what we described above Attrill (2010) describes as hot plasma channeled along loops, in either case we are referring to an

intensity enhancement that traces out along loops. Finally, in the case of Li et al. (2012) the reported reflection occurs very close to the limb and after close inspection of that region it is difficult to tell if this could be attributed to hot plasma, density enhancement, a transverse/kink-mode wave traveling along the loops, and/or if this is a true reflection.

3.3. Kinematics of the "Transmitted Wave" Front

Besides the reflection at the CH boundary, our full Sun movies show another interesting, and quite unique interaction between the wave and the CH—a wave transmission. The top center and right panel of Figure 6 show the appearance of a wave at the western part of the CH, first seen at 02:05 UT within the FOV of EUVI-A (Figure 11, top panel). This wave front wraps around the CH boundary and lies clearly ahead of the EUV wave that propagates northwest (NW) of the CH. In other words, the part of the wave that goes through the CH appears to *accelerate* relative to the part that propagates in the quiet Sun. This observation is fully consistent with the behavior of a fast-mode wave since the fast-mode speed will be higher in a CH (due to its reduced plasma density) than in the quiet Sun at a given height.

As was first introduced in Section 3.1, an apparent transmission of the primary wave is seen to occur across the CH. Here, we take another great circle slice toward the southwest (SW) originating at the flare site with a width of 18.6 arcsec within the FOV of AIA, labeled as "C" in Figure 3. Stack plots of the four AIA channels are plotted together in Figure 12. This slice passes over the CH region, bound by two horizontal red lines at 26° and 45° in the 193 Å plot. The velocity of the front before reaching the CH boundary and through the CH is measured independently using the AIA 193 Å observations. The velocity of the primary front was found to be 760 ± 40 km s^{-1}, and the front through the CH was 780 ± 20 km s^{-1}. As before, the error was estimated from making the fit 10 times. These measurements do not seem to be significantly different and so it seems that the front propagates continuously across the CH boundary. The
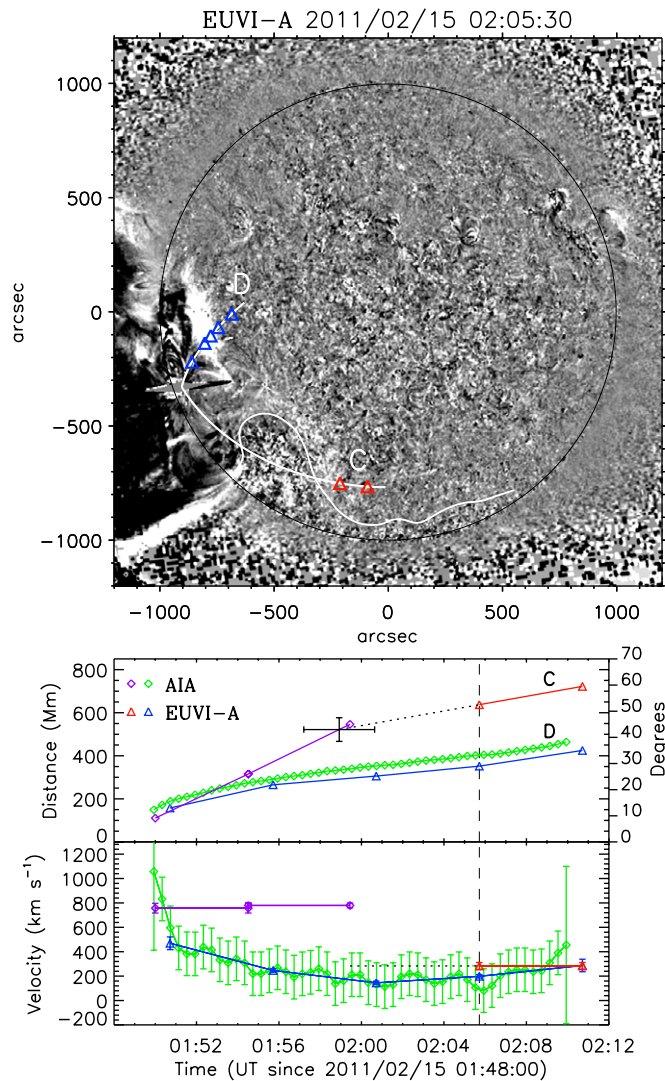
Figure 11. Top panel is an EUVI-A 195 Å running ratio frame taken at 02:05 UT. The coronal hole boundary outline is overlaid. The two great circle paths (C and D) used to make the kinematic measurements are shown. The bottom two panels are the distance–time and velocity plots. Path C is the same as that plotted in Figure 12, with AIA plotted piecewise. Diamonds (green and violet) were measured with AIA observations; triangles (red and blue) were measured with EUVI-A.

(A color version of this figure is available in the online journal.)

fact that the primary front velocity is comparable to the velocity within the CH can be understood as the primary front being initially driven by the CME to the CH boundary, upon which time a freely propagating fast-mode wave traverses the CH, and that coincidentally the velocity of the primary front and the fast-mode speed within the CH are similar. This scenario fits within the context of the hybrid interpretation of EUV waves. It could be that the primary front observed is the CMEs outer envelope or pseudo-wave, as proposed by Schrijver et al. (2011), and that upon reaching the CH a freely propagating fast-mode wave is launched through the CH, since pseudo-waves are not thought to cross into CHs.

The same scaling was applied throughout the AIA 193 Å stack plot and it is seen that once the front reaches the CH its intensity increases by a few percent, probably because it is projected against the dimmer CH. This interpretation is further reinforced by the AIA 171 Å observations that show a dimming

outside the CH and a transition to an enhancement. The intensity enhancement is much smaller in 171 Å because of the much smaller contrast of CH in that AIA passband. Because we are looking at the CH from an oblique angle toward the southern limb, we are likely seeing the temporary pileup at the wave front against the faint CH. With the EUVI-A observations only two usable data points were found at 02:05 UT (52.°5) and 02:10 UT (59.°5), they are overplotted in Figure 11 in which the front is clearly discernible SW of the CH. An error of 0.°5 was estimated for the two data points. A linear fit to these two data points yields a velocity 280 ± 30 km s^{-1}. The fit is extrapolated to meet the fit of the front through the CH as measured with AIA. Taking into account the error estimates, the EUVI-A fit intersects the AIA fit at $45° \pm 5°$ at 01:59 UT ± 1.7 minutes. This point, with error bars, is plotted in Figure 12 along with the fits and the two EUVI-A data points. From this, we conclude that what we are seeing within the CH is most likely the wave front and that upon exiting the CH and entering the quiet-Sun region, it attains the velocity of the local fast-mode wave speed there.

Next, it is explicitly shown that the wave front toward the SW propagates ahead of the front toward the NW by comparing their kinematics. Slice C and a track toward the NW lying over the quiet-Sun region, labeled "D" in Figures 3 and 11, are compared. This track is assumed to be a great circle originating at the flare site. The bottom two panels of Figure 11 show the kinematics of both the C and D tracks. The track C measurements were described above and also plotted in Figure 12, the (violet) diamonds are AIA piecewise measurements, and the (red) triangles are the two data points measured with EUVI-A. Also plotted is the point where the EUVI-A fit intersects the AIA fit and the dotted line is the extrapolation. Along track D, we were fortunate to have been able to make measurements in both AIA and EUVI-A. The (green) diamonds are AIA, and the (blue) triangles are EUVI-A measurements. An error of 0.°5 was estimated for both measurements. Looking at the plots, it is seen that the the two measurements from perpendicular vantage points are in agreement, especially in velocity (derived using three-point Lagrangian interpolation). The discrepancy seen in the distance measurements can simply be attributed to projection effects between the two spacecrafts. Comparing the position of the wave front at 02:05:43 UT, the front along the direction of track C has clearly propagated further away from the flare site than the front along track D by ∼285 Mm or ∼23.°5. Furthermore, it is seen that tracks C and D have decelerated to comparable velocities on the order of ∼300 km s^{-1}.

4. CONCLUSION AND DISCUSSION

We have demonstrated the wave nature of the coronal wave observed during the 2011 February 15 event by explicitly identifying and analyzing observations of secondary waves, which can be interpreted as reflection from and/or transmission through a CH. The asymptotic velocities, interpreted as reaching the local fast-mode speed, for all the wave ground track slices presented are comparable with each other (see Table 1). The difference in the asymptotic speeds of the "reflected" waves, slice "A" (380 versus 280 km s^{-1}), of the meridional track toward the north, slice "B" (260 km s^{-1}), and of the SW track (280 km s^{-1}), which crossed the CH, seem to reflect the variations of the local fast-mode speed in the corona and are in agreement with global MHD models (e.g., Schmidt & Ofman 2010; Zhao et al. 2011). Furthermore, these differences may provide good diagnostics for coronal seismology (e.g., Yang & Chen 2010; West et al. 2011), but this topic is outside of
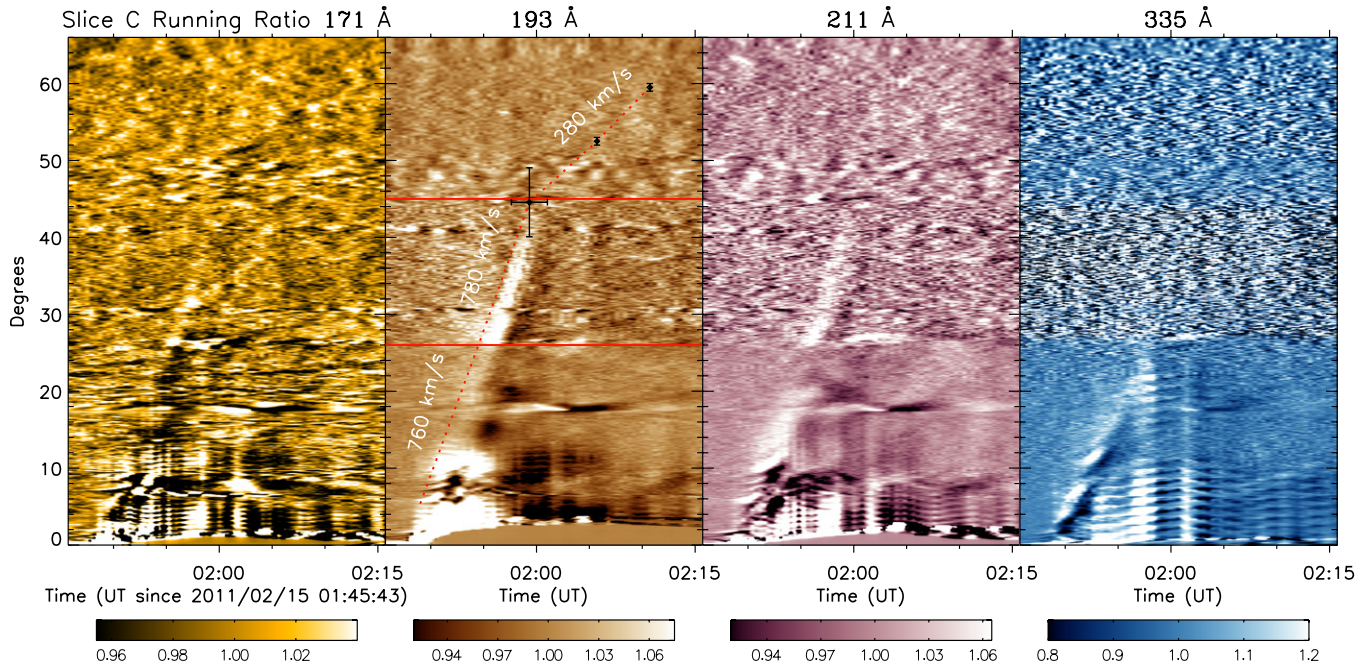
Figure 12. Slice "C," which demonstrates transmission, originates at the flare site and passes over the coronal hole toward the southwest. All four AIA channels are shown. The two red horizontal lines overlaid on the AIA 193 Å plot at 26° and 45° indicated the bounds of the coronal hole.

(A color version of this figure is available in the online journal.)

Table 1
Measured Velocities Along the Three Ground Track Slices

	Initial	Asymptotic
Slice A	1500 km s^{-1} east (see Figures 9 and 10)	280 km s^{-1} east 380 km s^{-1} west
Slice B	720 km s^{-1} north 740 km s^{-1} south	260 km s^{-1} north
Slice C	760 km s^{-1} southwest 780 km s^{-1} transmitted	280 km s^{-1} southwest

Notes. Initial refers to the initial velocity; for slice A this refers to the velocity of the wave upon being launched by the cascading loops, and for slice B and slice C refers to the velocity of the primary wave soon after the flare onset. Asymptotic refers to the velocity attained after some time up to the point where the wave is no longer measurable.

the scope of this paper. Our results are also consistent with other authors; for example, Warmuth & Mann (2011) showed, based on a statistical study, that coronal waves with initial fast velocities ($v \geqslant 320$ km s^{-1}) show the greatest deceleration and attain final velocities between 200 and 300 km s^{-1}, Veronig et al. (2010) found an asymptotic velocity of a coronal wave far from its origin of $\sim$280 km s^{-1}, and Long et al. (2008, 2011) found deceleration in the events that they studied. This can be explained if the coronal wave were in fact a freely propagating fast-mode MHD wave (e.g., Warmuth et al. 2004; Veronig et al. 2010; Long et al. 2011; Warmuth & Mann 2011). Warmuth & Mann (2011) proposed that for fast events ($v \geqslant 320$ km s^{-1}) the physical nature of the coronal wave can be explained as being initially a large-amplitude nonlinear wave and/or shock, presumably driven by the CME, that subsequently evolves (and decelerates) to a linear fast-mode wave propagating at the characteristic wave speed. This interpretation is in agreement with the hybrid view of coronal waves, in which the pseudo-wave can explain the outer envelope of the CME that drives a

fast-mode wave that is left freely propagating close to the solar surface once the CME has propagated radially away. It is this fast-mode wave that we are referring to in this paper.

We have reported on features which appear to obey the law of reflection. Close inspection of the reflection to the east into the FOV of EUVI-B shows that the secondary wave observed may have been triggered by a cascading loop arcade. To the west, into the FOV of EUVI-A, a secondary wave propagates along a path that seems to obey the law of reflection. But, is what is seen to the west in fact an observation of reflection? Or is it a secondary wave launched by the active region or the CH resonating? It is difficult to tell with these observations because in that region there are bright active region loops and the cadence of EUVI-A is not sufficient to resolve the fine temporal structure in that region. Our work presented a case of reflection in which a different approach was taken by evoking the law of reflection and ray tracing possible trajectories of the wave toward and reflecting from the CH boundary. We used both running and base ratio stack plots as appropriate. While the reflection is a strong argument for the wave nature of coronal waves, it has been challenged as an artifact of the data analysis method (Attrill 2010 but see counter arguments in Zhukov 2011). When it comes to these techniques, the primary problem arises when analyzing a stack plot that is placed between the active region that launched the coronal wave and reflecting CH boundary surface. Two such possible effects may cause misleading effects to be seen in the stack plots. The first could be hot plasma, density enhancement, and/or a transverse/kink-mode wave traveling along the loops aligned between the active region that launched the coronal wave and the CH boundary (Attrill 2010; Attrill et al. 2009). The second could be loops triggered to oscillate along the CH boundary resulting in a signature in the stack plot that appears like reflection. Of course, we must not be too hasty and dismiss the possibility that the wave did in fact reflect; the point we are trying to make is that each case of reflection should be considered carefully.

The transmitted wave toward the SW can be identified in both running and base ratio images without ambiguity because it propagates across the "pristine" quiet Sun. This is the first time, to our knowledge, that such a feature is identified in observations. The observation of the CH crossing (or transmission) is a very strong argument for the wave nature of these EUV disturbances. Until now, it has been reported based on empirical evidence that coronal waves do not traverse CHs (e.g., Thompson et al. 1999; Veronig et al. 2006; Attrill et al. 2007b; Ma et al. 2009). However, transmission has been discussed in the simulations of Schmidt & Ofman (2010), who also discuss it in terms of waves launched by the "resonating" of the CH. Nevertheless, we think that the same effect (e.g., transmission) is occurring in this event (whether by resonance is not clear and neither could it be determined based on these observations alone). Furthermore, we do see secondary waves launched all along the boundary of that CH (see associated movies), even beyond the reach of the original coronal wave, meaning that those waves would have had to cross the CH. But why has it not been observed before? We think that the size of the CH is likely the determinant factor. If the CH is large then the resonance may die out before it reaches the side opposite to the wave impact. On the other hand, if a hole is small the resonance may be sufficient to launch the secondary wave on the opposite side or all around the hole as suggested by Schmidt & Ofman (2010) and seen in this event as well as (partially) seen in the 2007 May 19 event (Gopalswamy et al. 2009).

The reflection and transmission observations are hard to reconcile with a pure pseudo-wave interpretation and our results provide further evidence in favor for the wave nature of coronal waves. But note that it is the fast-mode wave that we are referring to originally driven by the CME, whose outer envelope may be described by the pseudo-wave. It may be the case that for weaker events a fast-mode wave is not triggered or is triggered but has an amplitude that does not produce enough heating to be detected, in these cases a pure pseudo-wave interpretation may be appropriate as the CME and its outer envelope may be the only signatures observed. In other similar events to the one studied here, the 2011 June 7 event reported by Cheng et al. (2012) and the 2010 June 13 event reported by Ma et al. (2011) and Downs et al. (2012), it is shown that the coronal wave event is a composite phenomenon comprised of a CME that drives a fast-mode wave, giving further evidence to the hybrid interpretation. Based on those results what we have presented here is a detailed account of the wave component, initially driven by the CME, and that a pseudo-wave component should exist but the point at which one can distinguish between the two is not readily possible only to say that it should be early on in order to account for the secondary wave effects presented. We estimate that for this event the separation should have occurred sometime before 02:00 UT based on the fact that the transmission is observed to occur after that time, and transmission is purely a wave effect.

A projection effect of the CME material over the CH is the most obvious suggestion for the EUV emission inside the CH, which could be the projection of deflected coronal material by the CME toward the south. But the CME material propagates away from the CH (toward the ecliptic plane) and its southern flank stops at the boundary (Schrijver et al. 2011). Even if we assume that the expanding material is somehow tilted to the SW (as seen from Earth), it is difficult to account for the appearance of a propagating low coronal feature outside of the CH to the SW (seen in the FOV of EUVI-A). The CME field lines cannot penetrate through the CH. No such observations have even been reported in countless limb observations of CMEs. The reflection is an additional problem. There is no secondary CME; we use both running and base ratio images and we do not track the reflection back through the incident path (as was done by Gopalswamy et al. 2009 and Li et al. 2012), so there is no chance for confusion. Secondary waves can also be seen in AIA observations of the CME and coronal wave event on 2011 June 7 (Li et al. 2012) and a transmitted wave can be seen in the 2011 February 24 CME.

Instead, the fast-mode interpretation neatly accounts for all observations. Wave reflection is expected due to the sharp change in plasma parameters at the CH/quiet-Sun interface as has been simulated (Schmidt & Ofman 2010) and reported observationally (Long et al. 2008; Gopalswamy et al. 2009; Li et al. 2012), and wave transmission is predicted by MHD simulations (Schmidt & Ofman 2010). Moreover, oscillations of loops have also been reported as due to primary coronal wave fronts (e.g., Aschwanden & Schrijver 2011), which, as was shown here, can trigger secondary waves interpreted as being fast-mode MHD.

In summary, we have undertaken a detailed analysis of the global kinematics of an EUV wave using the full Sun coverage afforded by the *STEREO* and *SDO* missions and have found several important results:

1. Secondary wave effects attributed to the interaction of the primary coronal wave with the CH were described, including reflection and the first detection of wave transmission though a CH.
2. We report detailed observations of the interaction of a coronal wave with a loop arcade that straddles the boundary of a CH, which subsequently launches a secondary wave, whose trajectory resembles the law of reflection. Such observations have not been reported before and suggest an origin of secondary waves that appear as reflections launched by CHs.
3. Our observations and kinematic analysis are fully consistent with MHD simulations of fast-mode waves and suggest that these waves are initially driven, presumably by the expanding CME, but eventually relax to a freely propagating wave traveling at the local fast-mode speed.
4. Our analysis shows that the quiet Sun MHD wave speed can have modest variations.
5. We also report the first global measurements of the angular extent of EUV waves, which reached at least or approximately 200° before becoming too diffuse to be detected.

REFERENCES

Aschwanden, M. J., & Schrijver, C. J. 2011, ApJ, 736, 102

Attrill, G. D. R. 2010, ApJ, 718, 494

Attrill, G. D. R., Engell, A. J., Wills-Davey, M. J., Grigis, P., & Testa, P. 2009, ApJ, 704, 1296

Attrill, G. D. R., Harra, L. K., van Driel-Gesztelyi, L., & Démoulin, P. 2007a, ApJ, 656, L101

Attrill, G. D. R., Harra, L. K., van Driel-Gesztelyi, L., Démoulin, P., & Wülser, J.-P. 2007b, Astron. Nachr., 328, 760

Beauregard, L., Meetu, V., & Carsten, D. 2012, Astron. Nachr., 333, 125

Biesecker, D. A., Myers, D. C., Thompson, B. J., & Vourlidas, A. 2002, ApJ, 569, 1009

Chen, P. F., Fang, C., & Shibata, K. 2005, ApJ, 622, 1202

Chen, P. F., & Wu, Y. 2011, ApJ, 732, L20

Chen, P. F., Wu, S. T., Shibata, K., & Fang, C. 2002, ApJ, 572, L99

Cheng, X., Zhang, J., Olmedo, O., et al. 2012, ApJ, 745, L5

Cliver, E. W., Laurenza, M., Storini, M., & Thompson, B. J. 2005, ApJ, 631, 604

Cohen, O., Attrill, G. D. R., Manchester, W. B., & Wills-Davey, M. J. 2009, ApJ, 705, 587

Delaboudiniére, J.-P., Artzner, G. E., Brunaud, J., et al. 1995, Sol. Phys., 162, 291

Delannée, C., Török, T., Aulanier, G., & Hochedez, J.-F. 2008, Sol. Phys, 247, 123

Downs, C., Roussev, I. I., van der Holst, B., et al. 2011, ApJ, 728, 2

Downs, C., Roussev, I. I., van der Holst, B., Lugaz, N., & Sokolov, I. V. 2012, ApJ, 750, 134

Gallagher, P. T., & Long, D. M. 2011, Space Sci. Rev., 158, 365

Gilbert, H. R., & Holzer, T. E. 2004, ApJ, 610, 572

Gilbert, H. R., Holzer, T. E., Thompson, B. J., & Burkepile, J. T. 2004, ApJ, 607, 540

Gopalswamy, N., Yashiro, S., Temmer, M., et al. 2009, ApJ, 691, L123

Gosain, S. 2012, ApJ, 749, 85

Howard, R., Moses, J. D., Vourlidas, A., et al. 2008, Space Sci. Rev., 136, 67

Hudson, H. S., Khan, J. I., Lemen, J. R., Nitta, N. V., & Uchida, Y. 2003, Sol. Phys., 212, 121

Hudson, H. S., & Warmuth, A. 2004, ApJ, 614, L85

Jiang, Y., Zheng, R., Yang, J., et al. 2012, ApJ, 744, 50

Kaiser, M. L., Kucera, T. A., Davila, J. M., et al. 2008, Space Sci. Rev., 136, 5

Khan, J. I., & Aurass, H. 2002, A&A, 383, 1018

Klassen, A., Aurass, H., Mann, G., & Thompson, B. J. 2000, A&AS, 141, 357

Kosovichev, A. G. 2011, ApJ, 734, L15

Kozarev, K. A., Korreck, K. E., Lobzin, V. V., Weber, M. A., & Schwadron, N. A. 2011, ApJ, 733, L25

Lemen, J. R., Title, A. M., Akin, D. J., et al. 2011, Sol. Phys., 275, 17

Li, T., Zhang, J., Yang, S., & Liu, W. 2012, ApJ, 746, 13

Liu, W., Nitta, N. V., Schrijver, C. J., Title, A. M., & Tarbell, T. D. 2010, ApJ, 723, L53

Long, D. M., Gallagher, P. T., McAteer, R. T. J., & Bloomfield, D. S. 2008, ApJ, 680, L81

Long, D. M., Gallagher, P. T., McAteer, R. T. J., & Bloomfield, D. S. 2011, A&A, 531, A42

Ma, S., Raymond, J. C., Golub, L., et al. 2011, ApJ, 738, 160

Ma, S., Wills-Davey, M. J., Lin, J., et al. 2009, ApJ, 707, 503

Moreton, G. E., & Ramsey, H. E. 1960, PASP, 72, 357

Moses, D., Clette, F., Delaboudinière, J.-P., et al. 1997, Sol. Phys., 175, 571

Narukage, N., Hudson, H. S., Morimoto, T., et al. 2002, ApJ, 572, L109

O'Dwyer, B., Del Zanna, G., Mason, H. E., Weber, M. A., & Tripathi, D. 2010, A&A, 521, A21

Ofman, L. 2007, ApJ, 655, 1134

Ofman, L., & Thompson, B. J. 2002, ApJ, 574, 440

Patsourakos, S., & Vourlidas, A. 2009, ApJ, 700, L182

Patsourakos, S., & Vourlidas, A. 2012, Sol. Phys., in press (arXiv:1203.1135)

Patsourakos, S., Vourlidas, A., Wang, Y.-M., Stenborg, G., & Thernisien, A. 2009, Sol. Phys., 259, 49

Petrie, G. J. D. 2012, Sol. Phys., in press (arXiv:1202.4192v1)

Pohjolainen, S., Maia, D., Pick, M., et al. 2001, ApJ, 556, 421

Schmidt, J. M., & Ofman, L. 2010, ApJ, 713, 1008

Schrijver, C. J., Aulanier, G., Title, A. M., Pariat, E., & Delannée, C. 2011, ApJ, 738, 167

Stenborg, G., & Cobelli, P. J. 2003, A&A, 398, 1185

Thompson, B. J., Gurman, J. B., Neupert, W. M., et al. 1999, ApJ, 517, L151

Thompson, B. J., & Myers, D. C. 2009, ApJS, 183, 225

Thompson, B. J., Plunkett, S. P., Gurman, J. B., et al. 1998, Geophys. Res. Lett., 25, 2465

Thompson, W. T. 2006, A&A, 449, 791

Uchida, Y. 1968, Sol. Phys., 4, 30

van Driel-Gesztelyi, L., Attrill, G. D. R., Démoulin, P., Mandrini, C. H., & Harra, L. K. 2008, Ann. Geophys., 26, 3077

Veronig, A. M., Muhr, N., Kienreich, I. W., Temmer, M., & Vršnak, B. 2010, ApJ, 716, L57

Veronig, A. M., Temmer, M., Vršnak, B., & Thalmann, J. K. 2006, ApJ, 647, 1466

Veronig, A. M., Temmer, M., Vršnak, B., & Thalmann, J. K. 2008, ApJ, 681, L113

Vršnak, B., Magdalenić, J., Temmer, M., et al. 2005, ApJ, 625, L67

Vršnak, B., Warmuth, A., Brajša, R., & Hanslmeier, A. 2002, A&A, 394, 299

Vršnak, B., Warmuth, A., Temmer, M., et al. 2006, A&A, 448, 739

Wang, H., Shen, C., & Lin, J. 2009, ApJ, 700, 1716

Wang, S., Liu, C., Liu, R., et al. 2012, ApJ, 745, L17

Wang, Y.-M. 2000, ApJ, 543, L89

Warmuth, A. 2010, Adv. Space Res., 45, 527

Warmuth, A., & Mann, G. 2011, A&A, 532, A15

Warmuth, A., Mann, G., & Aurass, H. 2005, ApJ, 626, L121

Warmuth, A., Vršnak, B., Magdalenić, J., Hanslmeier, A., & Otruba, W. 2004, A&A, 418, 1101

West, M. J., Zhukov, A. N., Dolla, L., & Rodriguez, L. 2011, ApJ, 730, 122

White, R. S., & Verwichte, E. 2012, A&A, 537, A49

White, S. M., & Thompson, B. J. 2005, ApJ, 620, L63

Wills-Davey, M. J., & Attrill, G. D. R. 2009, Space Sci. Rev., 149, 325

Wills-Davey, M. J., DeForest, C. E., & Stenflo, J. O. 2007, ApJ, 664, 556

Wills-Davey, M. J., & Thompson, B. J. 1999, Sol. Phys., 190, 467

Wu, S. T., Zheng, H., Wang, S., et al. 2001, J. Geophys. Res., 106, 25089

Wuelser, J. P., Lemen, J. R., Tarbell, T. D., et al. 2004, Proc. SPIE, 5171, 111

Yang, H. Q., & Chen, P. F. 2010, Sol. Phys., 266, 59

Zhao, X. H., Wu, S. T., Wang, A. H., et al. 2011, ApJ, 742, 131

Zhukov, A. N. 2011, J. Atmos. Terr. Phys., 73, 1096

Zhukov, A. N., & Auchére, F. 2004, A&A, 427, 705